Analytica Chimica Acta 1276 (2023) 341632

Contents lists available at ScienceDirect

Analytica Chimica Acta

journal homepage: www.elsevier.com/locate/aca

Multi-analytical characterization of an oncoid from a high altitude hypersaline lake using techniques employed in the Mars2020 and Rosalind Franklin missions on Mars

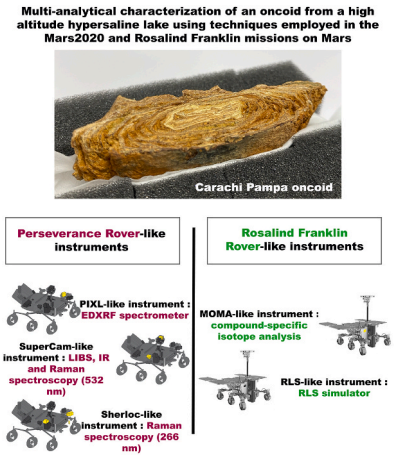
J. Huidobro [a,*], J.M. Madariaga [a], D. Carrizo [b], J.L. Laserna [c], F. Rull [d], J. Martínez-Frías [e], J. Aramendia [a], L. Sánchez-García [b], L. García-Gómez [c], F.A. Vignale [f], M.E. Farías [g], M. Veneranda [d], I. Población [a], L.M. Cabalín [c], G. López-Reyes [d], L. Coloma [a], C. García-Florentino [a], G. Arana [a], K. Castro [a], T. Delgado [c], C. Álvarez-Llamas [c], F.J. Fortes [c], J.A. Manrique [d], the SIGUE-Mars team

[a] IBeA Research Group, University of the Basque Country (UPV/EHU), Spain
[b] Centro de Astrobiología (CAB, INTA-CSIC), Spain
[c] LaserLab Research Group, University of Málaga (UMA), Spain
[d] ERICA Research Group, University of Valladolid (UVa), Spain
[e] Instituto de Geociencias (IGEO, CSIC-UCM), Spain
[f] European Molecular Biology Laboratory – Hamburg Unit, Notkestrasse, Germany
[g] PUNABIO S.A. Campus USP-T, San Pablo, Argentina

HIGHLIGHTS

- Astrobiogeochemical study of the Martian analog Carachi Pampa oncoid.
- Evaluation of terrestrial instruments analogous to those used on Mars.
- The MOMA-like instrument was the most appropriate for biosignature identification.
- Strong complementarity between Raman, IR, and XRF analysis of inorganic compounds.

GRAPHICAL ABSTRACT



ARTICLE INFO

Handling Editor: Xiu-Ping Yan

ABSTRACT

In this work, a geological sample of great astrobiological interest was studied through analytical techniques that are currently operating *in situ* on Mars and others that will operate in the near future. The sample analyzed

* Corresponding author. Department of Analytical Chemistry, University of the Basque Country (UPV/EHU), P.O. Box 644, E-48090, Bilbao, Spain.

https://doi.org/10.1016/j.aca.2023.341632
Received 24 January 2023; Received in revised form 26 June 2023; Accepted 13 July 2023
Available online 17 July 2023
0003-2670/© 2023 The Authors. Published by Elsevier B.V. This is an open access article under the CC BY-NC-ND license (http://creativecommons.org/licenses/by-nc-nd/4.0/).

Keywords:
Martian analog
Analytical techniques
Carachi pampa oncoid
Mars2020 mission
Rosalind franklin mission

consisted of an oncoid, which is a type of microbialite, collected in the Salar Carachi Pampa, Argentina. The main peculiarity of microbialites is that they are organo-sedimentary deposits formed by the *in situ* fixation and precipitation of calcium carbonate due to the growth and metabolic activities of microorganisms. For this reason, the Carachi Pampa oncoid was selected as a Martian analog for astrobiogeochemistry study. In this sense, the sample was characterized by means of the PIXL-like, SuperCam-like and SHERLOC-like instruments, which represent instruments on board the NASA Perseverance rover, and by means of RLS-like and MOMA-like instruments, which represent instruments on board the future ESA Rosalind Franklin rover. It was possible to verify that the most important conclusions and discoveries have been obtained from the combination of the results. Likewise, it was also shown that Perseverance rover-like remote-sensing instruments allowed a first detailed characterization of the biogeochemistry of the Martian surface. With this first characterization, areas of interest for in-depth analysis with Rosalind Franklin-like instruments could be identified. Therefore, from a first remote-sensing elemental identification (PIXL-like instrument), followed by a remote-sensing molecular characterization (SuperCam and SHERLOC-like instruments) and ending with an in-depth microscopic analysis (RLS and MOMA-like instruments), a wide variety of compounds were found. On the one hand, the expected minerals were carbonates, such as aragonite, calcite and high-magnesium calcite. On the other hand, unexpected compounds consisted of minerals related to the Martian/terrestrial surface (feldspars, pyroxenes, hematite) and organic compounds related to the past biological activity related to the oncoid (kerogen, lipid biomarkers and carotenes). Considering samples resembling microbialites have already been found on Mars and that one of the main objectives of the missions is to identify traces of past life, the study of microbialites is a potential way to find biosignatures protected from the inhospitable Martian environment. In addition, it should be noted that in this work, further conclusions have been obtained through the study of the results as a whole, which could also be carried out on Mars.

1. Introduction

Assessing the habitability of the Red Planet has been one of the main objectives for scientists for years. In fact, all Martian landing missions have tried to identify biosignatures on the surface or subsurface of the planet. This is the reason why the landing site of most of the surface missions were usually selected in areas where water was present at some point of the history of Mars.

The fact that ancient Mars was wet creates the possibility of habitability and the presence of microorganisms. However, under current Martian conditions, unprotected organic molecules would be degraded by one of the following destructive agents: (1) ultraviolet radiation, which would interact with the first millimeters of the regolith; (2) oxidation processes at the surface/subsurface, which could be efficient until 100 cm of depth depending on the characteristic of the materials; and/or (3) energetic particle of radiation from galactic cosmic rays, which would interact with organics in the first meters of depth [1].

Microbes can live in many environments, but those that live in extreme ones face inhospitable Martian conditions with different strategies, including formation of complex extremophile microbial communities that survive by light and water presence (O_2 availability). In this way, mats, biofilms, domes, endo-evaporitic mats and microbialites can be formed [2]. Therefore, these long-lived sedimentary structures are formed by the synergy between microbial metabolism and shallow water environments, such as salars, lagoons, and even volcanic fumaroles [3]. Geological records indicate that these communities dated to 3.5 billion years in age, thus, they are the main evidence of ancient life on Earth at that time [2,4]. Microbialites are organo-sedimentary deposits formed by sediment trapping, binding and *in situ* precipitation of calcium carbonate due to the growth and metabolic activities of microorganisms [2,5]. They can take the form of layered mounds, spheres, columns or sheet-like sediments that can be conical, domal, stratiform or branching [4].

Depending on their mesoscopic features, microbialites are classified into five groups: stromatolites, oncoids, thrombolites, dendrolites and leiolites. The main structures found on Earth are stromatolites, oncoids and thrombolites. Stromatolites display a laminated mesostructure, oncoids exhibit a concentrically laminated mesostructure and thrombolites show a clotted mesostructure [3,6].

On Earth, microbialites have been found along seashores and reefs, in fresh water lakes, lagoons and hypersaline lakes, salars and even volcanic fumaroles. In addition, they have been identified in lakes analogous to Martian paleolakes, such as Lake Thetis and other western Australian lakes [7,8]. In fact, microbialite-like structures were found by Opportunity [9], Spirit [10,11] and Curiosity [12] rovers on Mars. These facts support the use of a microbialite as a Martian analog.

Moreover, landing sites selected for the mentioned missions were directly related to past water scenarios, since they aimed to search for signs of ancient and present life in water environments on Mars [13,14]. Several billion years ago Jezero crater, the landing site of the Mars2020 rover, having a diameter of 47 km, was filled by a lake [14]. Oxia Planum, the landing site of Rosalind Franklin, is a 200-km wide low-relief terrain characterized by hydrous clay-bearing bedrock units and it is part of the major fluviodeltaic sedimentary system of the eastern margin of Chryse Planitia [13].

The aqueous past character of both sites makes an assumption about the presence of life, including protected life by bioprotectors like microbialites. If this happens, rovers may find them on the Martian surface and may analyze them by using their analytical payload.

Therefore, in order to serve as supportive science of the Mars2020 and Rosalind Franklin missions, a microbialite was characterized. Specifically, this sample was the Carachi Pampa oncoid, which was collected in the Salar Carachi Pampa (Catamarca, Argentina). This area is characterized by being an extreme environment at high altitude (3018 m above sea level), with high UV radiation exposition, high levels of desiccation, high daily temperature fluctuations and a different chemical composition of the water (e.g., high arsenic concentration) attributable to volcanic activity [3]. The novel characterization is based on the use of *in situ* analytical techniques that are currently being used on Mars and others that will be used in the near future. These techniques are part of the instruments of the Perseverance rover (Mars2020 mission) and of the Rosalind Franklin rover.

For biogeochemical characterization, the Planetary Instrument for X-ray Lithochemistry (PIXL) [15], SuperCam [16], Scanning Habitable Environments with Radar and Luminiscence for Organics and Chemicals (SHERLOC) [17], Raman Laser Spectrometer (RLS) [18] and the Mars Organic Molecule Analyzer [19] (MOMA)-like instruments were used.

The PIXL instrument, on board the Perseverance rover, can acquire high spectral resolution images of rock and soil chemistry. Over a period of several hours, the instrument can autonomously raster-scan an area of the rock surface and acquire a map composed of thousands of individual points. When correlated with visual image acquired by PIXL's camera, these maps reveal the distribution and abundance of chemical elements present in the rock [20]. The PIXL-like instrument selected in this work was the μ-EDXRF Tornado instrument, because both can acquire high spectral resolution observations of rock and soil chemistry. Moreover,

both instruments can correlate elemental results with visual images acquired with the instrument's camera, providing maps that can reveal the distribution and abundance of chemical elements making up the rock [15].

The SuperCam instrument, on board the Perseverance rover, is a remote mineral-identification instrument. It is equipped with several remote-sensing techniques: LIBS, visible and infrared (VNIR) reflectance spectroscopy and remote time-resolved Raman and luminescence spectroscopies [21].

In this sense, the LaserLab LIBS was used to recreate part of the SuperCam's measurements. This is because both use a laser with the same excitation wavenumber (1064 nm), although of different powers [16]. In order to simulate the SuperCam Raman measurement, the ERICA Raman spectrometer was used. This is because both are time-resolved spectrometers and both uses a single CCD detector to maximize the product of spectral range and resolution [22,23]. Morever, the VNIR ASD high-resolution FieldSpec4 spectroradiometer was used to recreate the SuperCam VNIR measurements. This instrument was used because it is portable and covers the spectral range of the SuperCam VNIR, which will go from 1300 to 2600 nm [24,25]. In order to complement the molecular data, the InVia Raman spectrometer was used to perform Raman imaging, but it should be highlighted that this equipment is not considered an analog of SuperCam. In order to simulate the SuperCam-Raman measurement, the ERICA Raman spectrometer was used. This is because both are time-resolved spectrometers and both uses a single CCD detctor to maximize the product of spectral range and resolution [22,23]. Moreover, the Raman contribution was complemented by images from the Renishaw InVia Raman spectrometer, but it should be noted that it is not a SuperCam analog [26].

The SHERLOC instrument, on board the Mars2020 rover, identifies potential biosignatures to understand the aqueous history of the Jezero region [27]. This instrument combines imaging with ultraviolet resonance Raman and native deep UV fluorescence spectroscopy. Although, there is no equipment on the market like SHERLOC, the SHERLOC-like instrument used in this work was the Horiba LabRam HR Evolution Raman spectrometer. This is because they both use a deep UV excitation laser to identify possible biosignatures [17]. SHERLOC uses a pulsed laser while the LabRam instrument has a continous wave laser. However, the Raman spectra obtained by both excitation lasers provide the same wavenumber for the Raman bands of compounds, although the form of the bands (intensity, HWMC, area) is slightly different.

The RLS instrument, on board the Rosalind Franklin rover, will provide geological and mineralogical information of igneous metamorphic and sedimentary processes, specifically regarding water-related interactions. It will contribute to the tactical aspects of exploration by providing a quick assessment of organic content before the analysis with MOMA [19,21]. The RLS-like instrument used in this work is the original prototype of the RLS. It is the RLS-Simulator instrument built by the University of Valladolid (UVa) research group [28].

Finally, the MOMA instrument, on board the Rosalind Franklin rover, was recreated to analyze organic molecules. This instrument, on board the Rosalind Franklin rover, is equipped with a gas chromatograph-mass spectrometer (GC-MS) and with a laser desorption-mass spectrometer (LDMS) to provide volatile and non-volatile molecules characterization of the drilled samples. MOMA will achieve the goal to search for molecular signs of past and present life on Mars [19]. In this work, the GC-MS and the GC-IRMS were seleceted as MOMA-like instrument because MOMA will use GC-MS for volatile molecule characterization and LDMS for non-volatile molecules. Although the same method was used for volatile molecules analysis, the technique for non-volatile molecules was not the same [19].

Taking all this into account, the aim of this work consists of analyzing and studying the benefits of using complementary analytical techniques for the characterization of non-terrestrial material of special biological interest. The analytical techniques used in this work were some that are already operating on Mars, those on board the Mars2020 rover, and others that will be in operation in the future, those on board the Rosalind Franklin rover.

2. Materials, methods and instrumentation

2.1. Salar carachi PAMPA oncoid

The sample was collected during a biogeochemical sampling campaign in January 2020 on the Salar Carachi Pampa, Catamarca, Argentina. A sample of about 28 g was collected with solvent-cleaned (dichloromethane and methanol) stainless-steel scraper, and transferred to polyethylene containers, where it was kept cold (~ 4 °C) until biogeochemical analysis in the laboratory. Fig. 1 shows the three sides of the microbialite or oncoid, whose dimensions are 51x31 × 16 mm.

2.2. PIXL-like instrument: μ-EDXRF spectrometer

Part of the elemental characterization was performed using both single point analysis and hyper map capabilities of the μ-EDXRF spectrometer M4 Tornado (Bruker Nano GmbH, Berlin, Germany). This instrument has a micro-focus side window Rh tube powered by a low-power HV generator and cooled by air that extends to a maximum current of 700 μA and voltage of 50 kV. It implements an XFlash silicon drift detector with 30 mm^2 sensitive area and energy resolution of 145 eV for Mn-K_α. The micrometric lateral resolution of the instrument, 25 μm for the Mo K_α-line, is achieved thanks to poly-cap optics. The spot size varies as a function of the energy, being 17 μm at 2.3 KeV and 32 μm at 18.3 KeV. The focusing process is supported by two video microscopes, one of them explores the sample under a low magnification (1 cm^2 area) while the other performs the final focusing (1 mm^2 area). As the instrument can detect elements with an atomic number (Z) higher than 10 (starting from Na), the measurements were performed under vacuum (20 mbar) to enhance the detection of the lightest elements. A deconvolution of the signals in the sum spectrum representing the whole mapped area was conducted automatically to construct the elemental images. After that, the distribution map of each element was represented as a function of the intensity of each detected element K_α line, except for Pb, using in this case the L_β line. The spectra acquisition and the image construction were performed using the M4 TORNADO software.

2.3. SUPERCAM-like instruments: Raman spectroscopy (532 nm laser), infrared (IR) spectroscopy and laser-induced breakdown spectroscopy (LIBS)

2.3.1. LIBS

For LIBS analysis, a pulsed laser beam (Big Sky, Q-switch Nd:YAG laser; @1064 nm; 8 ns pulse width, 40 mJ/pulse) was focused onto the

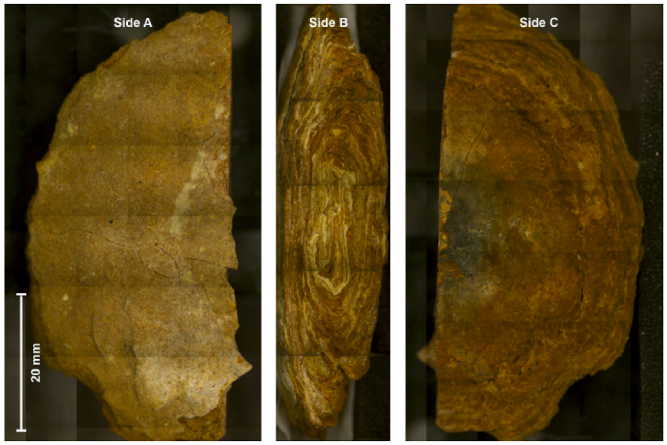


Fig. 1. Pictures of the three sides of the oncoid.

sample at normal incidence with a planoconvex quartz lens (Focal Length 100 mm). With this optical configuration, a 250 μm crater was generated on the sample surface. Plasma emission was collected at an angle of 90° with a 50 mm focal length fused-silica lens and focused onto the input aperture of a 1.5 m quadrifurcated optical fiber (1.5 m, ∅200 μm, Numerical Aperture of fiber optics = 0.22) coupled to the entrance slit of a four-channel Czerny-Turner spectrometer (Avantes 2048), providing a FWHM of 0.1 nm FWHM and a spectral range from 202 to 812 nm. Delay and integration time parameters were fixed at 1.28 μs and 1.1 ms, respectively. Time resolved studies were carried out using Andor iSTAR (DH740-25F-03) iCCD coupled to an Andor Shamrock SR-303i imaging spectrometer with a monochannel fiber. Temporal parameters were fixed to 17.5 μs and 50 μs (25 Gain) of delay and integration time respectively.

For microLIBS analysis, the optical configuration was slightly modified so that the focusing lens was replaced by a 15× microscope objective. With this LIBS system, a crater size of approximately 80 μm was promoted. The sample was placed in a XY manual linear stages and monitored using a Dino-Lite digital microscope in axial configuration.

2.3.2. IR spectroscopy (350–2500 nm)

Part of the molecular characterization was performed with VNIR spectroscopy by using the ASD high-resolution FieldSpec4 spectroradiometer (Analytical Spectral Devices Inc., Boulder, USA) equipped with the ASD probe for remote mode operations. The light source consisted of a halogen lamp (ASD Iluminator) placed at 30 cm of distance from the samples. The angle between the incident light and the sample, and that between the sample and the detector fiber was 45° in both cases. The fiber has an acceptance cone with an angle of 25° and was placed to a minimum distance of the sample to minimize the measurement surface. This device works in the 350–2500 nm wavelength range and uses three detectors for the different spectroscopic ranges: 350–1000 nm (silicon photodiode array for VNIR), 1001–1800 nm (InGaAs photodiode for SWIR1), and 1801–2500 nm (InGaAs photodiode for SWIR2). The FWHM is 3 nm in the visible region and 6 nm in the near infrared region. Sensor optimization and calibration were set with a Spectralon® white reference scanned once before each sample, and each spectrum is the result of the average of 10 scans. Spectra were collected with RS3 software (ASD Inc.), analyzed with the ViewSpecPro software (ASD Inc.), and compared with those found in the bibliography [29–31].

2.3.3. Raman spectroscopy (532 nm laser)

The molecular characterization was performed using two different Raman spectrometers; the Renishaw inVia confocal micro-Raman spectrometer (Renishaw, UK) and the microRaman built by the ERICA research group. On the one hand, the analyses with the Renishaw inVia were carried out both in single point mode and in the spectroscopic imaging mode. The instrument is equipped with a 785 nm (Renishaw, UK, RL785 with a nominal 45 mW out-put power) and 532 nm (Renishaw, UK, RL532C50 with a nominal 300 mW out-put power) excitation diode lasers and with a CCD detector cooled by Peltier effect. In addition, the instrument is coupled to a Leica DMLM microscope (Bradford, UK), implementing a XYZ Stage Control toolbar and equipped with a micro-camera for searching the points of interest. 5x N PLAN (0.12 NA), 20x N PLAN EPI (0.40 NA) lenses and 50x N PLAN (0.75 NA) long-range objective were used for visualization and focusing. The nominal power of the source can be modulated between 0,0001% and 100% of the total power to avoid thermo-decomposition of the sample. For this work, less than 20% was always used to preserve the sample. The spectra were obtained in the range of 150–1350 cm^{-1}, accumulating several scans from each spectrum to improve the signal-to-noise ratio.

Raman images were obtained using the high-resolution Stream LineTM setup (Renishaw, UK) coupled to the InVia Raman spectrometer. The control software moves the sample beneath the lens of the inVia's motorized microscope stage, so that the line is rastered across the region of interest with a spatial resolution up to 1 μm and moving in the snake mapping mode. The data are swept synchronously across the detector as the line moves across the sample and the spectra are read out continuously, recording a Raman spectrum at each pixel of the line raster. At the end, 2D Raman images are obtained containing individual Raman information at pixel level.

The InVia spectrometer was calibrated daily setting the 520.5 cm^{-1} silicon line. Data acquisition and treatment were carried out by the Wire™ 4.2 software package by Renishaw. The results were interpreted by comparing the collected Raman spectra with Raman spectra of pure standard compounds of the public databases RRUFF [32] and bibliography. The measurement parameters (laser, laser power, number of accumulations and the acquisition time of the spectra) were optimized for each analysis.

The ERICA microRaman was developed by assembling the following commercial components [33]: a Research Electro-Optics LSRP-3501 excitation laser (Helium–Neon) emitting at 633 nm, a KOSI Holospec 1.8i spectrometer, and an Andor DV420A-OE-130 CCD detector. The Nikon Eclipse E600 microscope coupled to the system is equipped with interchangeable long WD objectives of 5 × , 10 × , 20 × , 50 × , and 100 × . In this study, Raman data were collected from 25 different spots of interest that where visually selected by the operator. Spectra were recorded in the range between 130 and 3780 cm^{-1} by setting an acquisition time between 30 and 120 s, and a number of accumulations from 5 to 50.

2.4. SHERLOC-like instrument: Raman spectroscopy (266 nm laser)

The biomolecular characterization was performed using the LabRam HR Evolution Raman Spectrometer (Horiba, Japan). The analyses were carried out both in single point mode and in the spectroscopic imaging mode. The instrument is equipped with the 266 nm (mtb, CryLas, FQCW266 with a nominal 100 mW out-put power) excitation diode laser. In addition, the instrument is equipped with a Syncerity CCD detector and is coupled to a BXFM microscope (Olympus, Japan), implementing a Z motor and XY SCANplus 75x50 2 mm motorized microscope stage control toolbar (Märzhäuser Wetzlar, Germany) and equipped with a micro-camera for searching the points of interest. 5x MPlan N (0.10 NA, Olympus), 10x MPlan N (0.25 NA, Olympus) and 100x MPlan N (0.90 NA, Olympus) objectives were used for visualization and focusing the visible spectral range (785 nm laser), whereas the 74x UVI (0.66 NA, Horiba) objective was used for ultraviolet measurements. The nominal power of the source can be modulated between 0.01 and 100%. For this work, less than 20% was used to preserve the sample.

The spectra were obtained in the range of 100–4000 cm^{-1} in order to acquire organic bands and accumulating several scans from each spectrum to improve the signal-to-noise ratio. The measurement parameters (laser, laser power, number of accumulations and the acquisition time of the spectra) were optimized for each analysis.

The ultraviolet laser was calibrated daily setting the 1332.5 cm^{-1} diamond line. Data acquisition and treatment were carried out by the LabSpec 6.0 suit software by Horiba. The results were interpreted by comparing the collected Raman spectra with bibliography and with Raman spectra of pure standard compounds.

2.5. RLS-like instrument: RLS-simulator

The RLS-Sim was used to emulate the scientific outcome of the RLS as it is implemented on board the Rosalind Franklin rover [34]. The instrument is composed of the following commercial components: a BWN-532 excitation laser (B&WTek) emitting at 532 nm, a BTC162 high resolution TE Cooled CCD Array spectrometer (B&WTek) and an optical head with a long WD objective of 50 × . As presented in a dedicated manuscript [18], optical geometry, working distance (≈15 mm), laser power output (20 mW), FWHM (6–10 cm^{-1}) and spot size (≈50 μm) are closely resembling those of the RLS instrument. In addition to that, the RLS Simulator integrates the same algorithms the RLS will use on Mars

to autonomously perform sequential analyses, autofocus and optimization of the signal-to-noise ratio [35]. Using this instrument, a linear raster of 39 spots was carried out, thus simulating the nominal operation mode of the RLS.

Spectra visualization and treatment was carried out by the IDAT/SpectPro, a software developed by the RLS team to receive, decode, calibrate and verify the telemetries generated by the RLS on Mars [18]. Finally, data interpretation was performed by comparison with spectra of pure mineral phases from the Analytical Database of Martian Minerals (ADaMM) library [36].

2.6. MOMA-like instrument: lipid extraction, fractionation and analysis, both molecular and compound-specific isotopic

Lyophilized subsamples of the oncoid (i.e. internal and external layers) of ~5 g were extracted with a mixture of dichloromethane and methanol (DCM:MeOH, 3:1, v/v) by ultrasound sonication (3 cycles of 15 min). The concentrated total lipid extract was de-sulfured [37] and digested overnight at room temperature with potassium hydroxyde (6% MeOH, w/w) then separated into neutral and acidic fractions with *n*-hexane following the protocol by Grimalt et al. [38]. Further separation of the neutral fraction into non-polar (hydrocarbons) and polar (alcohols) sub-fractions was done according to procedures described elsewhere [39]. All three fractions were analyzed by gas chromatography mass spectrometry (GC-MS), by direct injection on hexane (non-polar fraction), or by injection after derivatization, with BF_3 in MeOH to form fatty acid methyl esters or FAMEs (acidic fraction) or with N,O-bis (trimethylsilyl) trifuoroacetamide (BSTFA) to form trimethylsilyl alcohols (polar fraction). GC-MS analysis was made using a 6850 GC system coupled to a 5975 VL MSD with a triple axis detector (Agilent Technologies) operating with electron ionization at 70 eV and scanning from m/z 50 to 650 [40]. Compounds identification was based on the comparison of mass spectra with reference materials and the NIST library (MSD ChemStation software), and their quantification on the use of external calibration curves of *n*-alkanes (C_{10} to C_{40}), FAMEs (C_8 to C_{24}) and *n*-alkanols (C_{14}, C_{16}, C_{18} and C_{20}). All chemicals and standards were supplied by Sigma Aldrich (San Luis, Missouri, USA). Recoveries of the internal standards averaged 69 ± 21%.

Carbon isotopic composition of individual lipids compounds were determined by coupling the GC-MS (Trace GC 1310 ultra/ICQ MS) to the isotope-ratio mass spectrometry system (MAT 253 IRMS, Thermo Fisher Scientific). Details on the analytical conditions, sample injection, analysis, and isotopic ratio calculations are provided elsewhere [41]. The isotopic values of the individual lipids separated by GC were calculated using CO_2 – spikes of known isotopic composition, introduced directly into the MS source, three times at the beginning and end of every run. Reference mixtures (Indiana University, USA) of known isotopic composition of *n*-alkanes (A6) and FAMEs (F8) were run every three samples in order to check the accuracy of the isotopic ratio determined by the GC-IRMS. For the alkanoic acids, the $\delta^{13}C$ data were calculated from the FAME values, correcting them for the one carbon atom added in the methanolysis [42].The stable-carbon isotopic composition was expressed as the $\delta^{13}C$ ratio, in per mile notation (‰) and relative to the Pee Dee Belemnite (PDB) standard.

3. Results and discussion

3.1. Results of the PIXL-like instrument

The μ-EDXRF instrument was used to perform elemental characterization. Figures S1, S2 and S3 show the μ-EDXRF imaging results for the main elements present in the three sides of the sample. The images were acquired with a motor step of 20 μm between every single measurement, ensuring that the sample was completely scanned.

The color intensity of the mapping for each element is directly correlated to the element concentration of the given elements on the analyzed sample. Thus, brighter color means higher relative presence of each element and vice versa, being the absence of the element represented with black. In this sense, when the elemental distribution of more than one element matches each other in the image, it is likely due to the presence of a mineral that contains both (or three, four, etc.) chemical elements (positive correlation). Thus, μ-EDXRF allows a) to ascertain the elemental composition of the samples, as well as b) to locate areas of potential minerals by analyzing the spatial distribution of the elements, and c) pre-sampling procedure for molecular analysis.

As Fig. S1 shows, the main element of side A is Ca, showing a wt.% higher than 67 among all the elements found (XRF cannot detect the very light elements like C, N, O, F, etc.). Fe, Si, Sr, Cl, Mg and Na are present in an abundance between 17 and 1 wt%. Finally, the composition is completed by traces of As, Al, S, K, Mn, P, Cu, Ti, Ni and Co at below 1 wt%.

After analyzing the elemental chemical images of Fig. S1, it can be seen that Na, the major element in the sample, is distributed over the entire surface. It is necessary to remember that one of the limitations of the μ-EDXRF is to not detect elements with an atomic number lower than that of Na, so it does not detect carbon. Carbon is one of the other elements expected to be found in abundance, as microorganisms form these types of structures by forming calcium carbonate layers.

Fig. S2 shows the elemental composition of side B. The elemental composition of this side is quite different from side A, since it has a lower Ca content (48.50 wt%) and higher content of other elements such as Fe (31.75 wt%). Each of the elements: Na, Si, Cl, Sr, As, Mg, S, K, Mn, Cu, P, Al, Ni and Ti has a relative abundance less than 5.5 wt%.

The distribution of chlorine, mainly in the core of the sample, is quite striking. This suggests that the early stages of oncoid formation, it was in chlorine-rich waters. What is also noteworthy is the high amount of iron and silicon on side B. This could be due to the presence of silicates and/or some oxide.

Fig. S3 shows the elemental composition of side C. In this case, the major element present in the sample was Fe (69.96 wt%), instead of Ca (13.16 wt%), which was the main element in A and B sides. Si, As, Cl, Sr, Mg, Na, Al, Cu, K, Mn, S, P, Ti and Ni were the minor elements, each of them having a relative abundance lower than 6 wt%.

Therefore, based on the elemental characterization, it can be said that side C is very different from the other two. Ca, which in the other two sides was a major component, is in lower relative concentration. Possibly, this is due to how the sample was rested in the field, as it will be explained below.

3.2. Results of the SuperCam-like instrument (LIBS, Raman and IR spectroscopies)

To complete the compositional characterization of the sample with the SuperCam-like instrument, LIBS, Raman and IR instruments were used. LIBS analysis was performed at 6 selected sampling positions on the oncoid surface. These positions were chosen according to the different colorations of the sample, which could suggest a distinction of composition. A photographic detail of the 6 sampling locations is shown in Fig. 2. LIBS analysis revealed the presence of emission lines for Ca (I) at 422.67 nm, Fe (I) at 404.58 nm, K (I) at 766.49 nm, Li (I) at 670.79 nm, Mg (I) at 285.21 nm, Mn (I) at 403.37 nm, Na (I) at 589.59 nm, Si (I) at 288.15 nm and Sr (I) at 460.73 nm in all the sampling positions.

Significant compositional differences were observed regarding minor elements such as Al (I), Ba (II), Cu (I), H_α, O and Ti (I) (see Table 1). In addition, the CaO molecular band, ranging from 590 to 625 nm, was also identified in the LIBS spectra.

For positions 1, 3 and 6, LIBS detection of atomic hydrogen and oxygen lines could indicate the presence of certain hydrated salts or hydrogen-carbonate in these points. A more exhaustive analysis was proposed to evaluate the elemental distribution along the growing axis of the microbialite sample. The sedimentary nature of the sample and its inherent roughness affected LIBS signal collection. To minimize the

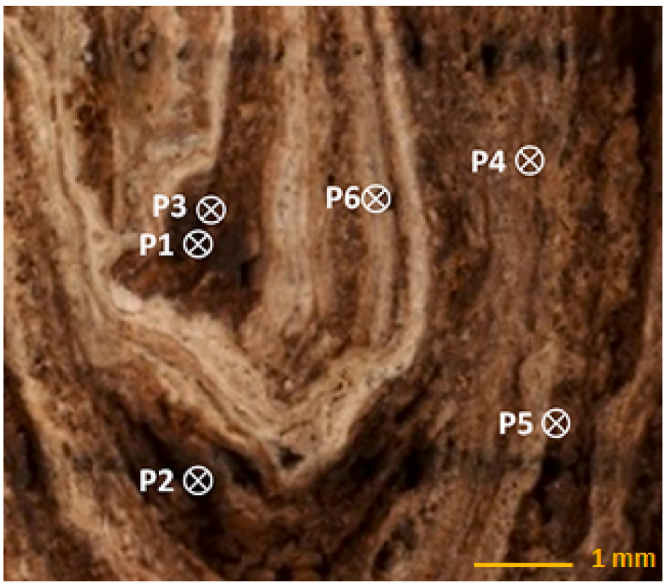


Fig. 2. Sampling positions analyzed by LIBS.

Table 1
Minor elements detected by LIBS of the 6 sampling positions.

Atomic element	Wavelength (nm)	P1	P2	P3	P4	P5	P6
Al	394.40	X	–	–	X	X	–
Ba	455.40	X	–	X	X	–	X
Cu	324.75, 327.39	X	–	X	X	–	X
H	656.28	X	–	X	–	–	X
O	777.19, 777.42, 777.54	X	–	X	–	–	X
Rb	780.03	X	X	X	X	–	X

fluctuations in the acquired signal and to reduce the laser energy oscillation caused by changes in the plasma temperature and amount of ablated material, each spectrum was normalized to the total intensity of the spectra. Normalized LIBS results are shown in Fig. 3.

The emission lines Na (I) 589.9 nm, Mg (I) 285.2 nm, Si (I) 288.2 nm, Ca (I) 422.7 nm, Fe (I) 404.6 nm and Sr (I) 460.7 nm were monitored along the growing axis. In addition, as commented above, spectra were normalized to unity. As shown, differences among elements are noticeable.

From data plotted in Fig. 3, a statistical study was performed using Pearson's correlation coefficients to verify the degree of variation between the input variables (see Fig. 4). Al and Ti were excluded, as they were not detected at all sampling points. As observed, in raster #1, Mg presents a high correlation with several other elements, with Pearson's correlation coefficient values close to 0.90 for Na, Si and Fe. However, correlation coefficients for raster #2 are better than for raster #1. For both rasters, Ca (the most abundant element) shows a higher correlation for all detected elements. It should be noted that when comparing to Fig. S2, Fe and Si have a similar spatial distribution. In Fig. 4 some negative correlations appear between variables, like for K that is distributed in different zones with respect to Ca, Fe or Si. This fact is consistent with μ-EDXRF results.

Due to the interest in detecting halogens Cl and F, the LIBS setup was modified. The atomic emissions of both elements have a lower relative intensity when compared to their potential molecular species, which produce an intense response even at low elemental concentrations. The detection strategy was focused on the identification of CaF ($B\ 2\Sigma^+ \rightarrow X\ 2\Sigma^+$, $\Delta v = 0$) and CaCl ($A^2\Pi \rightarrow X^2\Sigma$, $\Delta v = 0$) molecular bands. The formation of these molecular species takes place from recombination processes occurring during plasma cooling [43], thus requiring both longer delay and integration times [44]. In addition, the collection angle was adjusted to 45° with respect to the plasma expansion direction, which favors the sensitivity of the molecular emission signal. For comparative purposes, the acquired LIBS spectra were compared with different patterns of fluorite, aragonite and CaCl (see Fig. S4).

The CaF and CaCl molecular bands were analyzed in different spectral windows of the analyzed oncoid. Fig. 5 shows the chemical distribution of CaF and CaCl in different areas. The concentrations of chlorine and fluorine do not appear constant in the sample. Likewise, the dependence of the signal on the sample structure is evident.

The observed trend of each molecular emission, CaCl and CaF, was coincident with respect to the distribution of Ca in both spectral windows. The monitored Ca line was Ca(I) 611.76 nm for the CaCl spectral region and Ca(I) 526.56 nm for the CaF spectral region. The chlorine distribution was mainly located in the core of the sample and at one extreme side (see distance #11.5–14.5 mm). It must be considered that these data agree with the elemental maps for Cl obtained by μ-EDXRF. Moreover, fluorine seems to be located, at higher concentration, in the outermost zones of the sample. The fluorine data cannot be μ-EDXRF-checked because the atomic number of F is lower than that of Na.

With regard to Raman spectroscopy, the aim was to identify the spectra of expected compounds after analyzing the elemental data from the PIXL-like instrument and the combined technique with SuperCam-like instrument-LIBS. In this sense, the ERICA microRaman spectrometer was used.

As shown in Fig. 6 b, the spectral signatures of aragonite were detected in association with additional Raman peaks of its polymorph,

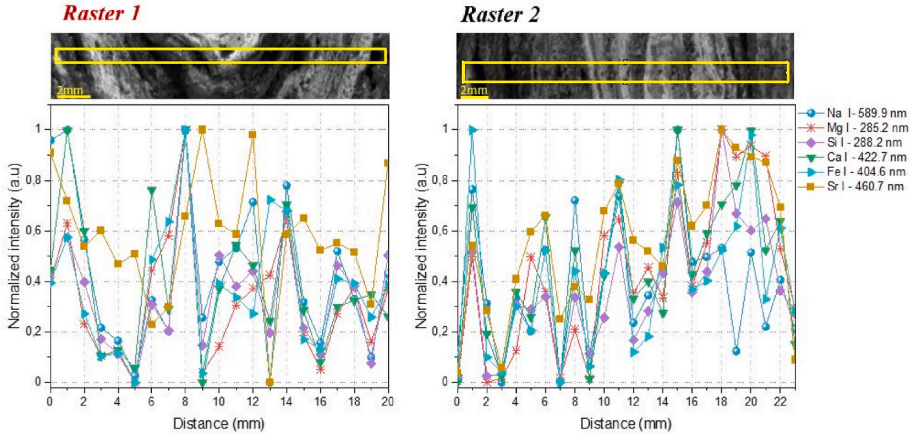


Fig. 3. Lateral profile of the major elements along raster 1 and 3 (20 and 23 positions, respectively) under atmospheric conditions, 15 laser shots per sampling position. Energy used was 40 mJ per pulse. Spatial resolution 1 mm.

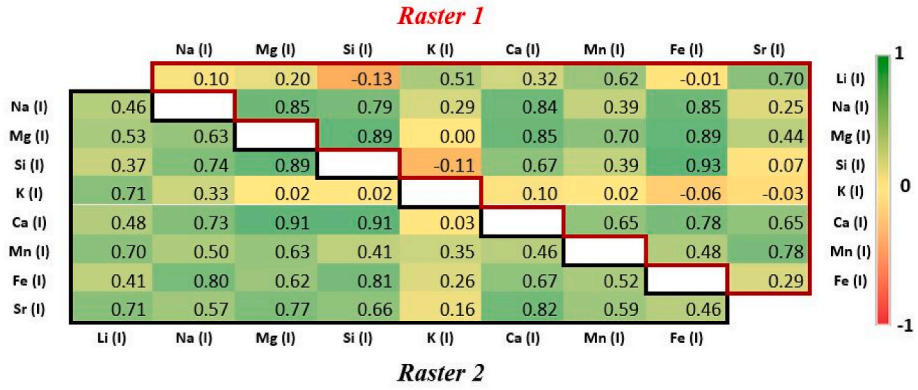


Fig. 4. Pearson correlations for detected elements in the two sampled areas. In the upper triangular matrix are the relationships obtained from the net intensity data, collected from the spectra normalized to the total area, over the 24 positions of raster 1. The lower triangular matrix shows the same data but for raster 2.

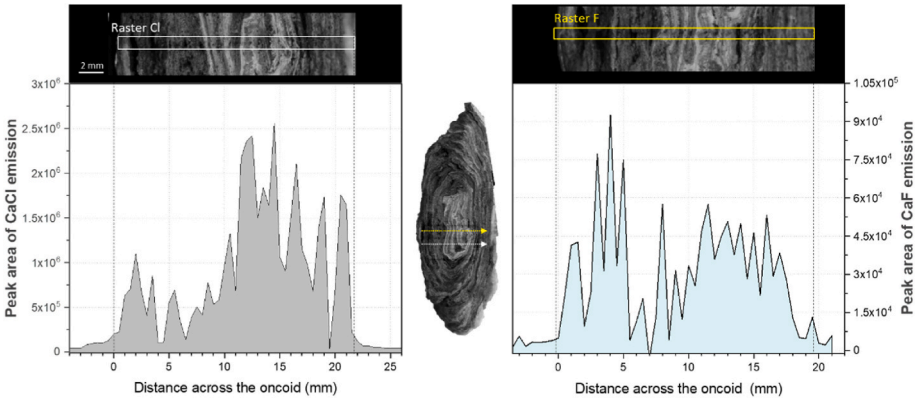


Fig. 5. Comparison between gray value profile and the intensity of the CaF ($B^2\Sigma^+ \rightarrow X\ ^2\Sigma^+$, $\Delta v = 0$), CaCl ($A^2\Pi \rightarrow X^2\Sigma$, $\Delta v = 0$) along of linear raster of 60 and 53 sampling locations, respectively, single shots per position. The energy used was 50 mJ per pulse. Spatial resolution 0.5 mm.

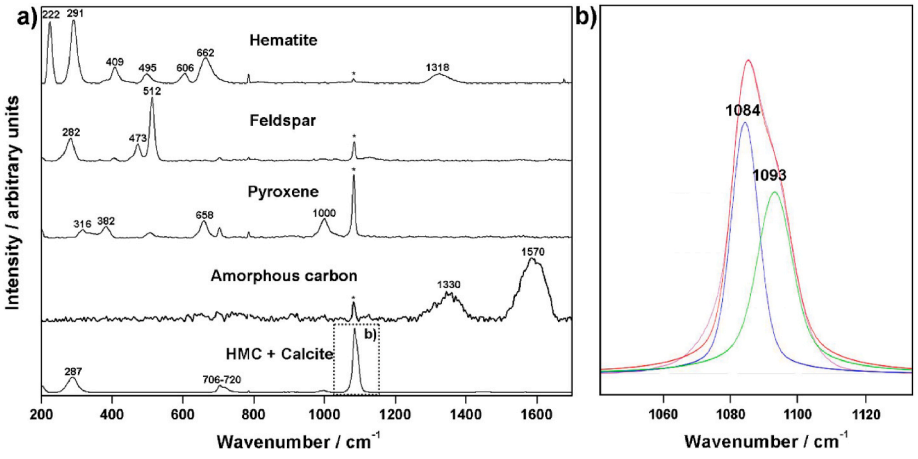


Fig. 6. a) Raman spectra of hematite, feldspar, pyroxene, kerogen, HMC and calcite, detected by the ERICA microRaman. b) Band deconvolution of the v1 band of $CaCO_3$ (purple: original spectra, blue: aragonite peak, green: calcite peak and red: deconvoluted spectrum). (For interpretation of the references to color in this figure legend, the reader is referred to the Web version of this article.)

calcite. Although aragonite forms the skeletal structure of microbialites, its preservation in this sample was relatively low. This could be a consequence of the fact that under ambient conditions and in the presence of water, aragonite transforms into its polymorph calcite, which is the most stable polymorph [45].

However, after band decomposition in pure Lorentzian-Gaussian bands of the non-symmetric experimental Raman band (Fig. 6 b), the main peak of calcite was found to be centered at 1093 cm^{-1}, which supposes a shifting of 6–7 cm^{-1} compared to nominal calcite standards. Similarly, secondary peaks also resulted shifted towards higher wavenumbers (from 281 to 286 cm^{-1} and from 711 to 720 cm^{-1} for lattice and ν_4 modes, respectively). As presented in previous works, peak shifting can be related to the cation substitution of Ca for Mg, which lead to the crystallization of the so-called high-magnesium calcite (HMC)

[46]. Knowing the linear correlation between peak shifting and magnesium substitution, that has been experimentally confirmed in previous works [47], it can be assumed that the calcite detected in this sample has a Mg content above 20 wt%. As reported elsewhere [48,49], the crystallization of HMC in water environment is often mediated by biological activity. Similarly, the simultaneous detection of HMC and aragonite is mostly found in biogenic structures, including oncoids. Considering the application of Raman spectroscopy in planetary missions, this result highlights the relevance of a high resolution mineral characterization of geological targets for astrobiology research.

Besides carbonate materials, Raman analysis also enabled the detection of two broad bands at 1330 and 1570 cm^{-1} fitting the D and G vibrational bands of the kerogen, a compound that can either be related to biotic or abiotic processes.

As shown in Fig. 6 a, pyroxene was also detected by its characteristic peaks at 315, 382, 658 and 1000 cm^{-1} [50]. According to the flow chart for pyroxene discrimination presented by Wang et al. [50], peak position indicated the detection of a monoclinic mineral phase (e.g. augite). The presence of minor amounts of feldspars was also confirmed by the detection of the main doublet at 473 and 512 cm^{-1}, followed by the secondary peak at 282 cm^{-1}. By comparing the spectrum displayed in Fig. 6 a with the reference pattern provided elsewhere [51], the detection of a K-feldspar (e.g. sanidine) was inferred. Finally, hematite inclusions were also found, as proved by the identification of Raman peaks at 222, 291, 409, 495, 606, 662 and 1318 cm^{-1} [51] in some of the studied spots.

The presence of pyroxene, feldspar and hematite could be related to the presence of soil remains on which the oncoid was formed [52]. In fact, after analyzing the high presence of iron in the C side of the oncoid (Fig. S3), it can be established that this side was the one in contact with the ground.

In order to complete the Raman analyses, another Raman instrument was used, the Renishaw InVia system. It should be noted that this instrument is not an analog to that of SuperCam and it was used just to complete the oncoid molecular characterization. In this way, most of the Raman spectra collected with this instrument possessed the characteristic bands that appear at 153 (m, medium), 206 (w, weak), 704 (w) and 1085 (vs, very strong) cm^{-1} [32], which match with the aragonite Raman bands. Fig. 7 shows the Raman spectrum of the aragonite found and its distribution along side B of the oncoid sample. The Raman image on that part of side B indicates that aragonite is only distributed in the lighter colored layers. However, single Raman analyses were performed on the dark layers and aragonite was also identified. The reason that the Raman image did not represent correctly the presence of calcium carbonate is due to the sample's relief. The dark areas are deeper than the light areas, which were well focused by the Raman spectrometer, while the dark ones were not.

In addition, thanks to these complementary Raman analyses, it was possible to detect a carotenoid through their main Raman bands detected at 959 (w), 1000 (m), 1151 (vs), 1193 (w), 1281 (w) and 1707 (vs) (Fig. S5). According to literature [53,54], this carotenoid is associated with halophilic archaeas. This finding links the oncoid to the place where it was found, that is, a salt-saturated lake, and explains the high presence of halogens, such as chlorine and fluorine, already detected by μ-EDXRF and LIBS.

3.3. Results of the SHERLOC-like instrument

Although SHERLOC is used to identify potential biosignatures and to understand the aqueous history of the Jezero region in the Mars2020 mission, the SHERLOC-like instrument showed no evidence of the existence of organics in the oncoid sample but did identify minerals that were previously found with the SuperCam-like Raman spectrometer.

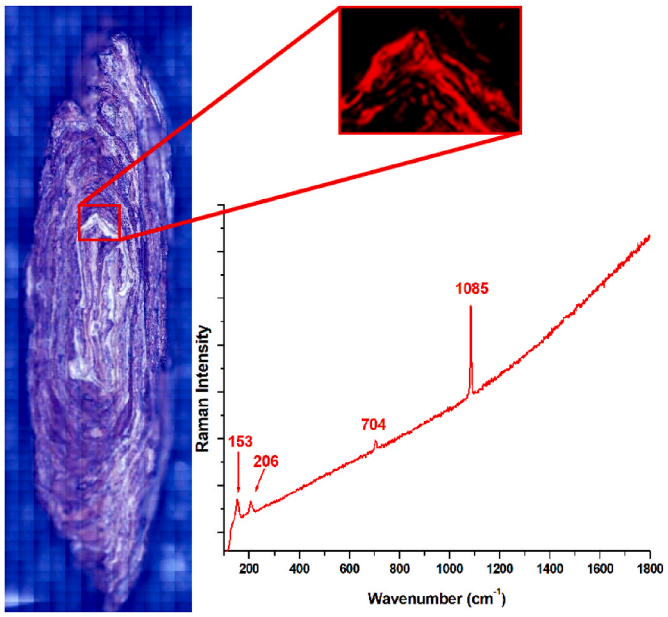


Fig. 7. Optical image, Raman image and Raman spectrum of the aragonite distribution in a small part of the side B of the sample, using the SuperCam-like instrument. The Raman image of aragonite was obtained using the interval 201-210 cm^{-1} that contains the one of the secondary Raman bands of aragonite. The Raman band at 1085 cm^{-1} was not selected, since calcite and aragonite overlap their main Raman band at this wavenumber. In this way, possible confusions of mineralogical distribution are avoided. Measurement parameters: 532 nm laser, grating 1800 l/mm (vis), 7 s of exposure time, 10% of laser power and objective 5×. The Raman map was obtained from a mosaic acquired with the Renishaw InVia microscope. This image is composed of 7980 points and was performed following the snake mapping mode.

3.4. Results of the RLS-Simulator instrument

The linear raster of 39 spots autonomously analyzed by the RLS-Sim, using the operational conditions constrained by the Rosalind Franklin mission, confirmed the results provided by the SuperCam-like instrument. Results indicated the presence of aragonite in most of the investigated spots through its Raman peaks (Fig. 8). In addition to this, calcite was also detected in some occasions (main peaks at 282 and 1085 cm^{-1}, see Fig. 8). Moreover, the presence of K-feldspars was also confirmed by the identification of the characteristic peaks at 283, 473 and 512 cm^{-1} (Fig. 8).

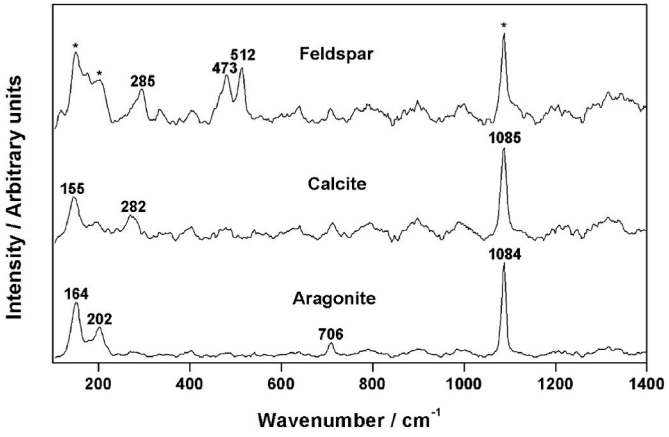


Fig. 8. Raman spectra of aragonite, calcite and feldspar, detected by the RLS-like instrument.

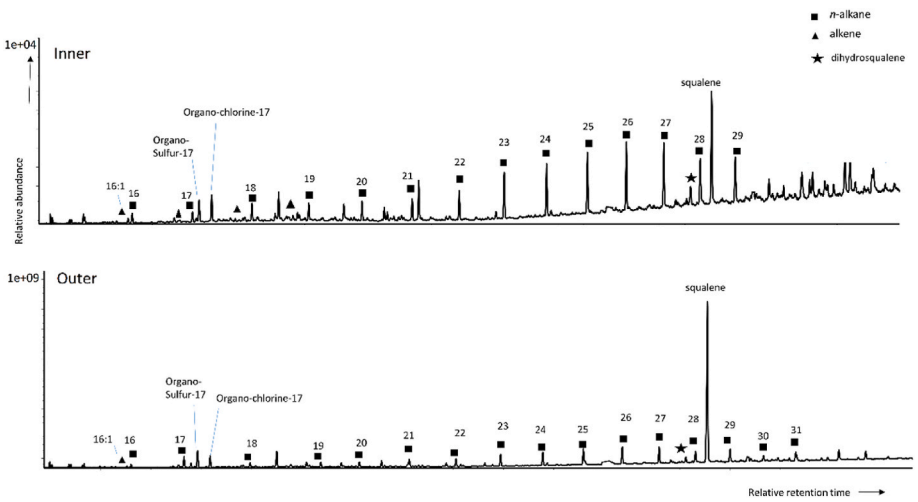


Fig. 9. Total ion chromatogram of the non-polar fraction in the inner and outer layer samples of the oncoid measured by the MOMA-like instrument. The different families of hydrocarbons are represented by different symbols. A complete list of compounds and their concentration is provided in Table S1.

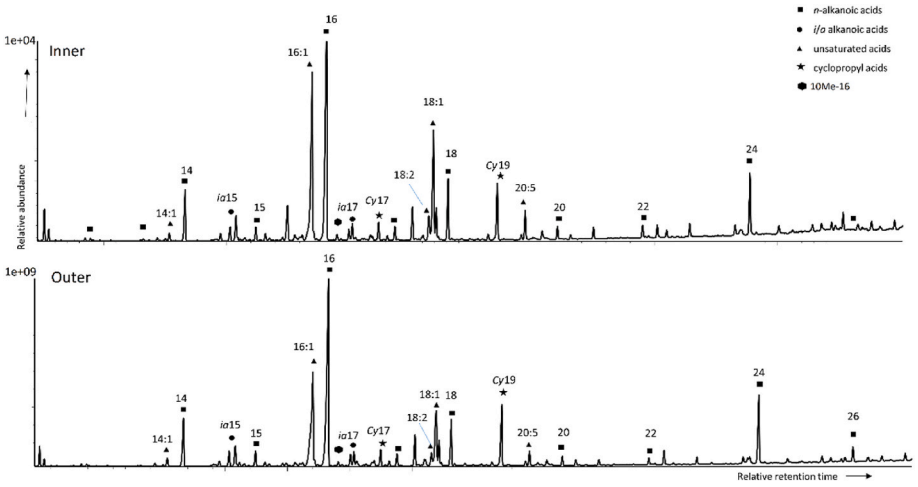


Fig. 10. Total ion chromatogram of the acid fraction from the inner and outer layers of the oncoid measured by the MOMA-like instrument. The different families of alkanoic acids are represented by different symbols. A complete list of compounds, details on nomenclature and their concentration is provided in Table S2.

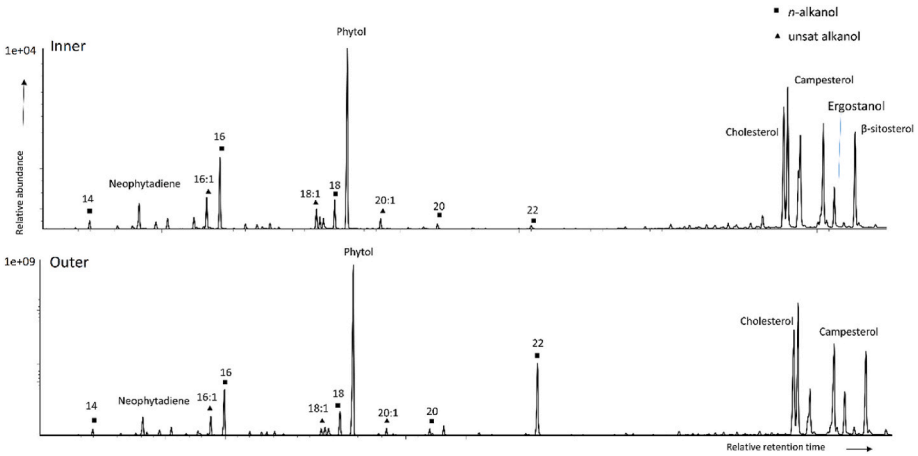


Fig. 11. Total ion chromatogram of the polar fraction from the inner and outer layers of the oncoid measured by the MOMA-like instrument. Different symbols over the peaks indicate the type of alcohol compound. A complete list of compounds, details on nomenclature and their concentration is provided in Table S3.

3.5. Results of the MOMA-like instrument

The molecular profile of lipid biomarkers (hydrocarbons, fatty acids, alkanols and sterols) was similar in the inner and outer oncoid layers (Figs. 9–11), but with concentrations an order of magnitude higher in the latter (Tables S1–S3). The relative abundance of lipids in the outer layer may be explained by their more recent synthesis relative to the older compounds preserved in the inner layer. Upon accretion, the oncoid mineral matrix would have favored the preservation of the entombed biomarkers from damaging UV radiation.

On both layers a wide variety of hydrocarbons were found in the non-polar fraction (Fig. 9), including a dominant series of *n*-alkanes from C_{15} to C_{31}, a few 1-alkenes ($C_{16:1}$, $C_{17:1}$, $C_{18:1}$ and $C_{19:1}$), an organo-sulfur compound (2, 5 di-*n*-alkylthiophene), an organochlorine heptadecane (Chloro-17), and isoprenoids (squalene and dihydrosqualene).

The acidic fraction was dominated by a series of *n*-alkanoic acids from $C_{12:0}$ to $C_{26:0}$ (mostly $C_{16:0}$), and some mono- ($C_{14:1[\omega5]}$, $C_{16:1[\omega7]}$, $C_{17:1[\omega7]}$, $C_{18:1[\omega7]}$ and $C_{18:1[\omega9]}$) and polyunsaturated alkanoic acids ($C_{16:2[\omega6]}$, $C_{18:2[\omega6]}$, $C_{20:4[\omega3]}$, and $C_{20:5[\omega3]}$), cyclopropyl-acids ($Cy_{17:0}$ and $Cy_{19:0}$), terminal branched (*iso/anteiso* $C_{15:0}$ and $C_{17:0}$) and other monomethyl (MMe) alkanoic acids (Fig. 10).

The polar fraction was dominated by phytol and relatives (neophytadiene and dihydrophytol), saturated alkanols from 14 to 22 carbons (C_{14} to C_{22}) and some of their monounsaturated homologs ($C_{16:1}$ and $C_{18:1}$), and sterols such as cholesterol, ergosterol and a few phytosterols (stigmasterol, campesterol and β-sitosterol, Fig. 11).

The lipid molecular profile of the oncoid suggested contribution from different prokaryotic and eukaryotic sources. On the one hand, the detection of short chain *n*-alkanes (C_{17}) and alkenes ($C_{16:1}$, $C_{17:1}$, $C_{18:1}$ and $C_{19:1}$) (Fig. 10) was related to oxygenic phototrophic cyanobacteria [55,56], whereas the detection of cyclopropyl nonadecanoic acid ($C_{19:0}$) was related to anoxygenic phototrophs such as purple sulfur bacteria (PSB) and/or green sulfur bacteria (GSB) [57]. On the other hand, the co-detection of the terminally branched *i/a*-$C_{15:0}$ and *i/a*-$C_{17:0}$, the cyclopropyl $Cy_{17:0}$, and the mid-chain branched 10Me–$C_{16:0}$ (Fig. 10) was associated with sulfate reducing bacteria [57–59].

In addition, biomass from phototrophic eukaryotes such as diatoms was deduced from the identification of the polyunsaturated alkanoic acids $C_{20:4}$ and $C_{20:5}$ [60]. The detection of the phytosterols campesterol, stigmasterol, and β-sitosterol support the microalgae inputs, although contribution from allochthonous sources (i.e. local higher plants) could also be possible. The relative abundance of photosynthetic microorganisms was supported by the relative abundance of phytol (i.e. a side chain of chlorophyll-*a*; Fig. 11) and the $\delta^{13}C$ values (26.2 to −35.6‰) measured for the lipids (Fig. S6), overall compatible with a carbon fixation by the Calvin−Benson−Bassham cycle [61] typically used by cyanobacteria, PSB, algae, and higher plants [62]. Still, the most depleted $\delta^{13}C$ values (lower than ca. −32‰) might represent the use of the alternative Wood-Ljungdahl (reductive acetyl CoA) pathway [63] by fermentative and acetogen SRB [62]. The biomarkers profile in the oncoid is comparable to that found in similar hypersaline settings in the Argentinean Andes and have been related to induced mineral precipitation of stromatolites in Andean lakes.

The detection of lipidic biomarkers by GC-MS is relevant for the search of organics on Mars. Lipids are ubiquitous and relatively more geostable biomolecules than others with potential to persist in the geological record for up to billions of years [64] under ideal conditions (i.e. mild diagenesis). They provide a testimony of life that can be unequivocal when their molecular detection is combined with their compound-specific isotopic analysis.

Mineral protection such as that exerted by aragonite in the oncoid sample can favor the preservation of biomarkers by acting as a shield of strong UV radiation or other aggressive environmental factors. Ideally, the SAM or MOMA instruments could detect organic signals in Martian settings harboring water bodies in the past similar to those described in this work. Thus, interpreting the molecular and isotopic lipid fingerprints in the oncoid provides insights for the interpretation of potentially similar signals in samples with comparable structure (stromatolitic) from Noachian Mars. In fact, the SAM instrument has already detected a number of short-chain hydrocarbons (C_{10}–C_{12}) at Gale crater [65] that have been hypothesized to be potential degradation products of carboxylic acids.

The plausible discovery of more short-chain lipids in other Martian samples highlights the need for further decoding of biomarker records in aquatic environments analogous to ancient Mars.

4. Discussion

By using all techniques described above, it was possible to verify that a good methodology in sample characterization consists of a first recognition by elemental techniques (PIXL and SuperCam-LIBS-like instruments), followed by a molecular characterization (SuperCam-IR, SuperCam-Raman, SHERLOC, RLS and MOMA-like instruments).

Elemental characterization allowed the identification of halogens inside the sample, forming the oldest materials. This fact indicates that in the first stages of the formation of the microbialite, the environment was aqueous, rich in salts. In addition, by identifying the distribution of elements across the sample (elemental mappings), it was possible to detect hotspots where more than one element coexisted. In this way, elemental techniques also gave clues about which minerals could possibly be found before the subsequent use of molecular analytical techniques. It should be noted that the first elemental characterization is very useful both for *in situ* analysis on Mars and for sample analysis in the laboratory.

Raman analyses performed with SuperCam, SHERLOC and RLS-like instruments revealed that the dominant mineral was aragonite. This data agreed with the elemental map of Ca obtained with the PIXL-like instrument. Besides, after performing a more detailed analysis, the SuperCam-Raman like instrument was able to detect minor compounds, such as calcite, HMC, feldspars, pyroxenes, kerogen and hematite. Calcite was likely present because under specific ambient conditions and in the presence of water, aragonite transforms into calcite, which is the most stable polymorph. It is worthy to point out that the presence of HMC is relevant from a biogeochemical point of view since the cation substitution of Ca for Mg may occur in aqueous environments dominated by biological activity. In this way, the finding of kerogen by Raman spectroscopy is also very relevant as it probes the presence of ancient carbonaceous material.

The abundances of Al, Si, Fe and other elements reflect the soil influence on which the oncoid was formed. This fact was also reflected in the detection of pyroxene, feldspar and hematite. In fact, after analyzing the high presence of iron in the C side of the oncoid, it was inferred that, this side was likely the one in contact with the ground.

As mentioned above, it should also be noted that the sample was cut, allowing access to side B for analysis. Taking into account that it is a soft carbonate sample, when it was split, material was removed, leaving holes that could not be detected by surface spectroscopic techniques, such as EDXRF, LIBS, IR and Raman. In response to this, spectroscopic images show dark areas that could not be focused with the microscope because the surface was not smooth and homogeneous. This fact and the complexity of the morphology of the sample was the reason why no new minerals could be identified with IR, as well as, organics with SHERLOC. It should be noted that, although the UV Raman laser is ideal for the identification of organic compounds, the low relative abundance of these compounds compared to mineral phases such as aragonite made their detection unlikely.

However, the SHERLOC's lack of organic compound findings was covered by MOMA-like instrument. It is known that the Salar Carachi Pampa is characterized by being a salt-saturated lake, where only extremophile microorganisms can live. In this sense, a wide variety of lipids and eukaryote biomarkers were found thanks to the MOMA-like instrument, which were similar to those reported for similar

hypersaline lakes from the same location.

5. Conclusion

After analyzing all the results obtained in this work, it was found that although some analytical techniques possess the same scientific basis, each one has a different scope. In any case, the study of non-terrestrial samples through the combination of all these techniques provides deeper and more precise information, since some are better for large-scale use, while others allow microscopic analysis.

In this sense, for a mineralogical characterization PIXL, SuperCam and RLS-like instruments were used. Based on the results obtained, PIXL is a suitable instrument to be used in the first contact with the area to be analyzed. This is because PIXL allows a quick and accurate elemental identification, with which the notion of space is not lost and, in addition, allows locating points of interest where certain elements coexists.

Once the points of interest were identified, SuperCam analyses were performed. On the one hand, SuperCam-LIBS provided a more detail elemental knowledge of the area, since instead of scanning and generating an image, LIBS makes shot-by-shot measurements, thus increasing accuracy but decreasing the working range.

On the other hand, the first molecular approximation was performed by using the SuperCam-IR and SuperCam-Raman techniques. It should be noted that both techniques, like SuperCam-LIBS, are remote-sensing techniques, which allow to identify the large-scale mineralogy of the surface. If the morphology of the sample is challenging, it does not allow the analysis of grains that are difficult to access, which is what happened in this work with IR analysis.

Thus, with the insight gained through this mineralogical characterization, it was possible to establish points of high interest for microscopic analysis. At this point, the RLS-like instrument was used for more in-depth characterization. This instrument required sample preparation by grinding, since it analyzes the samples at a microscopic scale and with low detection limits, enabling more precise mineralogical analysis.

By combining these three molecular techniques, results of great interest were obtained. This methodology is based on steps from larger to smaller scale in size. By first identifying areas of potential interest with the remote-sensing SuperCam techniques, it is possible to make more targeted measurements with the RLS, thus avoiding time-consuming sample collection and subsequent preparation.

The same happened with the instruments based on the identification of organic matter: SHERLOC and MOMA. In this work, it could be seen how SHERLOC is a remote-sensing technique without sample preparation. Since it is a Raman spectrometer, the laser only accesses the upper areas. In this sense, SHERLOC only identified aragonite, since the relative abundance of organic compounds was much lower compared to the main mineral phase.

However, in the same way as RLS, MOMA requires sample collection and preparation, analyzing the samples as a whole and allowing the identification of organic compounds. In this work, it could be seen how the SHERLOC lack of knowledge was covered by the analyses with MOMA, which provided a wide variety of results.

Table 2 lists all the characteristics of the instruments and analytical techniques used in this work with their details. In this table, it can be appreciated that the Perseverance techniques analyze on a large-scale, while those of Rosalind Franklin allow a microscopic analysis. Consequently, the Perseverance techniques allow a first approach, while the Rosalind Franklin techniques allow in-depth analysis.

Therefore, as stated in the discussion section, it is important to highlight that the results of the instruments should be analyzed as a whole, which can provide more relevant information than using only the data from one instrument. In this way, the lack of information generated by the drawbacks related to some instruments due to high detection limits and/or critical spectral resolutions, are complemented by the information coming from other instruments.

Thus, by combining the results obtained by as many analytical techniques as possible, more in-depth conclusions will be developed about the biogeochemistry of Mars. This study may also be useful for the design of scientific payloads for future landing missions.

In addition, taking into account that the high bombardment of ionizing particles from the Sun and stars, including ultraviolet radiation, causes the decomposition of any organic molecule. Thus, it would be interesting to evaluate the protective capacity of microbialites to preserve biosignatures against different intensities of ultraviolet radiation as future work.

Table 2
The analytical techniques used in this work, associated with the instruments on board the Perseverance and Rosalind franklin rovers, as well as the instruments used in terrestrial laboratories. In the details section, all the strengths and weaknesses of each instrument are indicated.

Rover	Analytical techniques	Corresponding instrument on Mars	Corresponding analog-instrument used on terrestrial laboratories	Details
Perseverance	EDXRF	PIXL	M4 Tornado EDXRF spectrometer	- Remote-sensing
	LIBS	SuperCam	LaserLab LIBS	- No sampling
	IR		ASD high-resolution FieldSpec4 spectroradiometer	- No sample preparation
	Raman		ERICA Raman spectrometer	- Hyperspectral maps (PIXL)
	Raman	SHERLOC	LabRam HR Evolution UV-laser Raman spectrometer	- Distribution
				- Semi-quantification (PIXL)
				- Quantification (LIBS)
				- Faster
				- First approach
				- Higher limit of detection
				- Large-scale
Rosalind Franklin	Raman	RLS	RLS-simulator	- No remote-sensing
	GC-MS	MOMA	GC-MS + GC-IRMS	- Inside the rover
				- Tedious
				- Sampling
				- Sample preparation
				- Homogenized sample
				- Semi-quantification (Raman)
				- Quantification (GC-MS)
				- Slower
				- Detailed study
				- Lower limit of detection
				- Micro-scale

CRediT authorship contribution statement

J. Huidobro: Conceptualization, Methodology, Investigation, Data curation, Writing – original draft, Writing – review & editing, Visualization. **J.M. Madariaga:** Conceptualization, Methodology, Writing – original draft, Writing – review & editing, Supervision, Project administration. **D. Carrizo:** Investigation, Data curation, Writing – original draft, Writing – review & editing. **J.L. Laserna:** Conceptualization, Methodology, Writing – review & editing, Supervision, Project administration. **F. Rull:** Conceptualization, Methodology, Writing – review & editing, Supervision, Project administration. **J. Martínez-Frías:** Conceptualization, Methodology, Writing – review & editing, Supervision, Project administration. **J. Aramendia:** Conceptualization, Methodology, Writing – review & editing. **L. Sánchez-García:** Investigation, Data curation, Writing – original draft, Writing – review & editing. **L. García-Gómez:** Writing – review & editing. **M. Veneranda:** Investigation, Data curation, Writing – original draft, Writing – review & editing. **I. Población:** Writing – review & editing. **L.M. Cabalín:** Writing – review & editing. **G. López-Reyes:** Writing – review & editing. **L. Coloma:** Writing – review & editing. **C. García-Florentino:** Writing – review & editing. **G. Arana:** Writing – review & editing. **K. Castro:** Writing – review & editing. **T. Delgado:** Investigation, Data curation, Writing – original draft, Writing – review & editing. **C. Álvarez-Llamas:** Writing – review & editing. **F.J. Fortes:** Writing – review & editing. **J.A. Manrique:** Writing – review & editing.

Declaration of competing interest

The authors declare the following financial interests/personal relationships which may be considered as potential competing interests: Jennifer Huidobro reports article publishing charges was provided by University of the Basque Country. Jennifer Huidobro reports equipment, drugs, or supplies was provided by University of the Basque Country.

Data availability

Data will be made available on request.

Acknowledgements

This work is part of the common activities of the "Thematic Network SIGUE-Mars" (Grant RED2018-102600-T, funded by the Spanish AEI/MICINN/FEDER) who funded the coordination actions until the final editing of the manuscript. The costs of the research works were covered by two projects: (1) the Raman On Mars project: "Contribution of the Raman spectroscopy to the exploration of Mars and Martian Moons: ExoMars, Mars 2020 and MMX missions (RamOnMars)" (Grant No. PID2019-10744RB-C31, funded by the Spanish Agency for Research AEI/MICINN/FEDER); and (2) the PAMMAT project "Alteration processes in Mars and Moon Meteorites, and terrestrial Analogues at different environments: Mars2020, Rosalind Franklin and Returned Samples from Mars and Moon" (Grant No. PID2022-142750OB-I00, funded by the Spanish Agency for Research AEI/MICINN/FEDER).

In addition, all the authors would like to thank Luis Ahumada and Nicolás Lopez for their assistance in the field trips and to the native communities of Antofalla, El Peñón, and Antofagasta de la Sierra. Finally, authors want to thank the Comunidad de Antofalla and the Secretaría de Medio Ambiente de la provincial de Catacarma for providing the exploration permits.

Appendix A. Supplementary data

Supplementary data to this article can be found online at https://doi.org/10.1016/j.aca.2023.341632.

References

[1] O. Poch, A. Noblet, F. Stalport, J.J. Correia, N. Grand, C. Szopa, P. Coll, Chemical evolution of organic molecules under Mars-like UV radiation conditions simulated in the laboratory with the "Mars organic molecule irradiation and evolution" (MOMIE) setup, Planet, Space Sci. 85 (2013) 188, https://doi.org/10.1016/j.pss.2013.06.013.

[2] M.E. Farías, L.A. Saona-Acuña, Modern microbial mats and endoevaporite systems in andean lakes: a general approach, in: M.E. Farías (Ed.), Microb. Ecosyst. Cent. Andes Extrem. Environ., Springer International Publishing, Cham, 2020, pp. 21–28, https://doi.org/10.1007/978-3-030-36192-1.

[3] F.A. Vignale, A.I. Lencina, T.M. Stepanenko, M.N. Soria, L.A. Saona, D. Kurth, D. Guzmán, J.S. Foster, D.G. Poiré, P.G. Villafañe, V.H. Albarracín, M. Contreras, M.E. Farías, Lithifying and non-lithifying microbial ecosystems in the wetlands and salt flats of the central Andes, Microb. Ecol. 83 (2022) 1, https://doi.org/10.1007/s00248-021-01725-8.

[4] R.G. Joseph, O. Planchon, N.S. Duxbury, K. Latif, G.J. Kidron, L. Consorti, R. A. Armstrong, C. Gibson, R. Schild, Oceans, lakes, and stromatolites on Mars, Adv. Astron. 2020 (2020) 1, https://doi.org/10.1155/2020/6959532.

[5] R.V. Burne, L.S. Moore, Microbialites: organosedimentary deposits of benthic microbial communities, Palaios 2 (1987) 241, https://doi.org/10.2307/3514674.

[6] R. Riding, Microbialites, stromatolites, and thrombolites, in: J. Reitner, V. Thiel (Eds.), Encycl. Geobiol. Encycl. Earth Sci. Ser., Springer, 2011, pp. 635–654, https://doi.org/10.1007/978-1-4020-9212-1_196.

[7] N. Planavsky, K. Grey, Stromatolite branching in the Neoproterozoic of the Centralian Superbasin, Australia: an investigation into sedimentary and microbial control of stromatolite morphology, Geobiology 33 (2007), https://doi.org/10.1111/j.1472-4669.2007.00116.x.

[8] L. Xiao, J. Wang, Y. Dang, Z. Cheng, T. Huang, J. Zhao, Y. Xu, J. Huang, Z. Xiao, G. Komatsu, A new terrestrial analogue site for Mars research: the Qaidam Basin, Tibetan Plateau (NW China), Earth Sci. Rev. 164 (2017) 84, https://doi.org/10.1016/j.earscirev.2016.11.003.

[9] G. Bianciardi, V. Rizzo, N. Cantasano, Opportunity rover's image analysis: microbialites on Mars? Int. J. Aeronaut. Sp. Sci. 15 (2014) 419, https://doi.org/10.5139/IJASS.2014.15.4.419.

[10] G. Bianciardi, V. Rizzo, Microbialites at gusev crater, Mars, J. Astrobiol. Outreach. 3 (2015), 1000143, https://doi.org/10.4172/2332-2519.1000143.

[11] S.W. Ruff, J.D. Farmer, Silica deposits on Mars with features resembling hot spring biosignatures at El Tatio in Chile, Nat. Commun. 7 (2016), 13554, https://doi.org/10.1038/ncomms13554.

[12] A.M.T. Elewa, Fossils on Mars: a brief review of the evidence, J. Astrobiol. 7 (2021) 29.

[13] C. Quantin-Nataf, J. Carter, L. Mandon, P. Thollot, M. Balme, M. Volat, L. Pan, D. Loizeau, C. Millot, S. Breton, E. Dehouck, P. Fawdon, S. Gupta, J. Davis, P. M. Grindrod, A. Pacifici, B. Bultel, P. Allemand, A. Ody, L. Lozach, J. Broyer, Oxia planum: the landing site for the ExoMars "Rosalind franklin" rover mission: geological context and prelanding interpretation, Astrobiology 21 (2021) 345, https://doi.org/10.1089/ast.2019.2191.

[14] K.A. Farley, K.H. Williford, K.M. Stack, R. Bhartia, A. Chen, M. de la Torre, K. Hand, Y. Goreva, C.D.K. Herd, R. Hueso, Y. Liu, J.N. Maki, G. Martinez, R. C. Moeller, A. Nelessen, C.E. Newman, D. Nunes, A. Ponce, N. Spanovich, P. A. Willis, L.W. Beegle, J.F. Bell, A.J. Brown, S.-E. Hamran, J.A. Hurowitz, S. Maurice, D.A. Paige, J.A. Rodriguez-Manfredi, M. Schulte, R.C. Wiens, Mars 2020 mission overview, Space Sci. Rev. 216 (2020) 142, https://doi.org/10.1007/s11214-020-00762-y.

[15] A.C. Allwood, L.A. Wade, M.C. Foote, W.T. Elam, J.A. Hurowitz, S. Battel, D. E. Dawson, R.W. Denise, E.M. Ek, M.S. Gilbert, M.E. King, C.C. Liebe, T. Parker, D. A.K. Pedersen, D.P. Randall, R.F. Sharrow, M.E. Sondheim, G. Allen, K. Arnett, M. H. Au, C. Basset, M. Benn, J.C. Bousman, D. Braun, R.J. Calvet, B. Clark, L. Cinquini, S. Conaby, H.A. Conley, S. Davidoff, J. Delaney, T. Denver, E. Diaz, G. B. Doran, J. Ervin, M. Evans, D.O. Flannery, N. Gao, J. Gross, J. Grotzinger, B. Hannah, J.T. Harris, C.M. Harris, Y. He, C.M. Heirwegh, C. Hernandez, E. Hertzberg, R.P. Hodyss, J.R. Holden, C. Hummel, M.A. Jadusingh, J. L. Jørgensen, J.H. Kawamura, A. Kitiyakara, K. Kozaczek, J.L. Lambert, P. R. Lawson, Y. Liu, T.S. Luchik, K.M. Macneal, S.N. Madsen, S.M. McLennan, P. McNally, P.L. Meras, R.E. Muller, J. Napoli, B.J. Naylor, P. Nemere, I. Ponomarev, R.M. Perez, N. Pootrakul, R.A. Romero, R. Rosas, J. Sachs, R. T. Schaefer, M.E. Schein, T.P. Setterfield, V. Singh, E. Song, M.M. Soria, P.C. Stek, N.R. Tallarida, D.R. Thompson, M.M. Tice, L. Timmermann, V. Torossian, A. Treiman, S. Tsai, K. Uckert, J. Villalvazo, M. Wang, D.W. Wilson, S.C. Worel, P. Zamani, M. Zappe, F. Zhong, R. Zimmerman, PIXL: planetary instrument for X-ray Lithochemistry, Space Sci. Rev. 216 (2020) 134, https://doi.org/10.1007/s11214-020-00767-7.

[16] R.C. Wiens, S. Maurice, S.H. Robinson, A.E. Nelson, P. Cais, P. Bernardi, R. T. Newell, S. Clegg, S.K. Sharma, S. Storms, J. Deming, D. Beckman, A.M. Ollila, O. Gasnault, R.B. Anderson, Y. André, S.M. Angel, G. Arana, E. Auden, P. Beck, J. Becker, K. Benzerara, S. Bernard, O. Beyssac, L. Borges, B. Bousquet, K. Boyd, M. Caffrey, J. Carlson, K. Castro, J. Celis, B. Chide, K. Clark, E. Cloutis, E. C. Cordoba, A. Cousin, M. Dale, L. Deflores, D. Delapp, M. Deleuze, M. Dirmyer, C. Donny, G. Dromart, M.G. Duran, M. Egan, J. Ervin, C. Fabre, A. Fau, W. Fischer, O. Forni, T. Fouchet, R. Fresquez, J. Frydenvang, D. Gasway, I. Gontijo, J. Grotzinger, X. Jacob, S. Jacquinod, J.R. Johnson, R.A. Klisiewicz, J. Lake, N. Lanza, J. Laserna, J. Lasue, S. Le Mouélic, B. Lucero, J.M. Madariaga, M. Madsen, S. Madsen, N. Mangold, J.A. Manrique, J.P. Martinez, J. Martinez-Frias, K.P. McCabe, T.H. McConnochie, J.M. McGlown, S.M. McLennan, N. Melikechi, P. Meslin, J.M. Michel, D. Mimoun, A. Misra, G. Montagnac,

F. Montmessin, V. Mousset, N. Murdoch, H. Newsom, L.A. Ott, Z.R. Ousnamer, L. Pares, Y. Parot, R. Pawlucyk, C.G. Peterson, P. Pilleri, P. Pinet, G. Pont, F. Poulet, C. Provost, B. Quertier, H. Quinn, W. Rapin, J. Reess, A.H. Regan, A.L. Reyes-Newell, P.J. Romano, C. Royer, F. Rull, B. Sandoval, J.H. Sarrao, V. Sautter, M. J. Schoppers, S. Schöder, D. Seitz, T. Shepherd, P. Sobron, B. Dubois, V. Sridhar, M. J. Toplis, I. Torre-Fdez, I.A. Trettel, M. Underwood, A. Valdez, J. Valdez, D. Venhaus, P. Willis, The SuperCam instrument suite on the NASA Mars 2020 rover: body unit and combined system tests, Space Sci. Rev. 217 (2021) 4, https://doi.org/10.1007/s11214-020-00777-5.

[17] R. Bhartia, L.W. Beegle, L. DeFlores, W. Abbey, J. Razzell Hollis, K. Uckert, B. Monacelli, K.S. Edgett, M.R. Kennedy, M. Sylvia, D. Aldrich, M. Anderson, S. A. Asher, Z. Bailey, K. Boyd, A.S. Burton, M. Caffrey, M.J. Calaway, R. Calvet, B. Cameron, M.A. Caplinger, B.L. Carrier, N. Chen, A. Chen, M.J. Clark, S. Clegg, P. G. Conrad, M. Cooper, K.N. Davis, B. Ehlmann, L. Facto, M.D. Fries, D.H. Garrison, D. Gasway, F.T. Ghaemi, T.G. Graff, K.P. Hand, C. Harris, J.D. Hein, N. Heinz, H. Herzog, E. Hochberg, A. Houck, W.F. Hug, E.H. Jensen, L.C. Kah, J. Kennedy, R. Krylo, J. Lam, M. Lindeman, J. McGlown, J. Michel, E. Miller, Z. Mills, M. E. Minitti, F. Mok, J. Moore, K.H. Nealson, A. Nelson, R. Newell, B.E. Nixon, D. A. Nordman, D. Nuding, S. Orellana, M. Pauken, G. Peterson, R. Pollock, H. Quinn, C. Quinto, M.A. Ravine, R.D. Reid, J. Riendeau, A.J. Ross, J. Sackos, J.A. Schaffner, M. Schwochert, M. O Shelton, R. Simon, C.L. Smith, P. Sobron, K. Steadman, A. Steele, D. Thiessen, V.D. Tran, T. Tsai, M. Tuite, E. Tung, R. Wehbe, R. Weinberg, R.H. Weiner, R.C. Wiens, K. Williford, C. Wollonciej, Y.-H. Wu, R. A. Yingst, J. Zan, Perseverance's scanning habitable environments with Raman and luminescence for organics and chemicals (SHERLOC) investigation, Space Sci. Rev. 217 (2021) 58, https://doi.org/10.1007/s11214-021-00812-z.

[18] G. Lopez-Reyes, M. Veneranda, J.A. Manrique, Á. González Martín, A. Moral, C. Perez-Canora, J.A. Rodríguez Prieto, A. Sanz Arranz, J. Saiz Cano, E. Lalla, M. Konstantinidis, O. Prieto-Ballesteros, J. Medina, M.Á. González, E. Charro, J. M. Lopez, F. Rull, The Raman laser spectrometer ExoMars simulator (RLS Sim): a heavy-duty Raman tool for ground testing on ExoMars, J. Raman Spectrosc. 53 (2022) 382, https://doi.org/10.1002/jrs.6281.

[19] F. Goesmann, W.B. Brinckerhoff, F. Raulin, W. Goetz, R.M. Danell, S.A. Getty, S. Siljeström, H. Mibach, H. Steininger, R.D. Arevalo, J.A. Buch, C. Freissinet, A. Grubisic, U.J. Meierhenrich, V.T. Pinnick, F. Stalport, C. Szopa, J.L. Vago, R. Lindner, M.D. Schulte, J.R. Brucato, D.P. Glavin, N. Grand, X. Li, F.H.W. van Amerom, The Mars organic molecule analyzer (MOMA) instrument: characterization of organic material in martian sediments, Astrobiology 17 (2017) 655, https://doi.org/10.1089/ast.2016.1551.

[20] M.M. Tice, J.A. Hurowitz, A.C. Allwood, M.W.M. Jones, B.J. Orenstein, S. Davidoff, A.P. Wright, D.A.K. Pedersen, J. Henneke, N.J. Tosca, K.R. Moore, B.C. Clark, S. M. McLennan, D.T. Flannery, A. Steele, A.J. Brown, M.-P. Zorzano, K. Hickman-Lewis, Y. Liu, S.J. VanBommel, M.E. Schmidt, T.V. Kizovski, A.H. Treiman, L. O'Neil, A.G. Fairén, D.L. Shuster, S. Gupta, Alteration history of Séítah formation rocks inferred by PIXL x-ray fluorescence, x-ray diffraction, and multispectral imaging on Mars, Sci. Adv. 8 (2022), https://doi.org/10.1126/sciadv.abp9084.

[21] J. Huidobro, J. Aramendia, G. Arana, J.M. Madariaga, Reviewing in situ analytical techniques used to research Martian geochemistry: from the Viking Project to the MMX future mission, Anal. Chim. Acta 1197 (2022), 339499, https://doi.org/10.1016/j.aca.2022.339499.

[22] P. Bernardi, L. Parès, R. Newell, T. Nelson, O. Gasnault, J.-M. Réess, V. Schridar, I. Contijo, A. Reyes-Newell, G.E. Peterson, C. Legett, B. Dubois, S.H. Robinson, Optical design and performance of the SuperCam instrument for the Perseverance rover, in: Z. Sodnik, B. Cugny, N. Karafolas (Eds.), Int. Conf. Sp. Opt. — ICSO 2020, SPIE, 2021, p. 53, https://doi.org/10.1117/12.2599243.

[23] R.C. Wiens, R. Newell, S. Clegg, S.K. Sharma, A. Misra, P. Bernardi, S. Maurice, K. McCable, P. Cais, S.S. Teams, The SuperCam remote Raman spectrometer for Mars 2020, in: Lunar Planet. Sci. XLVIII, Abs, The Woodlands, TX, USA, 2017, p. 2600.

[24] J.M. Reess, M. Bonafous, L. Lapauw, O. Humeau, T. Fouchet, P. Bernardi, P. Cais, M. Deleuze, O. Forni, S. Maurice, S. Robinson, R.C. Wiens, S. Team, Greece, in: Int Conf, Sp Opt, Chania (Eds.), The SuperCam Infrared Instrument on the NASA Mars2020 Mission, vol. 11180, 2018. Abs 1118037-2.

[25] T. Fouchet, J.R. Johnson, O. Forni, J.M. Reess, P. Bernardi, R.T. Newell, A. Ollila, C. Legett, P. Beck, A. Cousin, C. Royer, C. Pilorget, F. Poulet, P. Pilleri, E.A. Cloutis, T. McConnochie, F. Montmessin, A.J. Brown, R. Wiens, S. Maurice, S.V.W. Group, SuperCam Visible/Near-Infrared spectroscopy onboard the Perseverance rover, No. 2548, in: 52nd Lunar Planet. Sci. Conf., Virtual Conference, 2021. Abs 1939.

[26] J. Huidobro, J. Aramendia, C. García-Florentino, P. Ruiz-Galende, I. Torre-Fdez, K. Castro, G. Arana, J.M. Madariaga, Mineralogy of the RBT 04262 Martian meteorite as determined by micro-Raman and micro-X-ray fluorescence spectroscopies, J. Raman Spectrosc. 53 (2022) 450, https://doi.org/10.1002/jrs.6291.

[27] J. Razzell Hollis, K.R. Moore, S. Sharma, L. Beegle, J.P. Grotzinger, A. Allwood, W. Abbey, R. Bhartia, A.J. Brown, B. Clark, E. Cloutis, A. Corpolongo, J. Henneke, K. Hickman-Lewis, J.A. Hurowitz, M.W.M. Jones, Y. Liu, J. Martinez-Frías, A. Murphy, D.A.K. Pedersen, S. Shkolyar, S. Siljeström, A. Steele, M. Tice, A. Treiman, K. Uckert, S. VanBommel, A. Yanchilina, The power of paired proximity science observations: Co-located data from SHERLOC and PIXL on Mars, Icarus 387 (2022), 115179, https://doi.org/10.1016/j.icarus.2022.115179.

[28] M. Veneranda, J. Sáiz, A. Sanz-Arranz, J.A. Manrique, G. Lopez-Reyes, J. Medina, H. Dypvik, S.C. Werner, F. Rull, Planetary terrestrial analogues library (PTAL) project: Raman data overview, J. Raman Spectrosc. 51 (2020) 1731–1749, https://doi.org/10.1002/jrs.5652.

[29] P. Ruiz-Galende, I. Torre-Fdez, J. Aramendia, L. Gomez-Nubla, K. Castro, G. Arana, S.F. Vallejuelo, M. Maguregui, J. Medina, V.G. Baonza, F. Rull, J.M. Madariaga, New Raman–visible near-infrared database of inorganic and mineralogical planetary and terrestrial compounds and its implications for Mars: phyllosilicates, J. Raman Spectrosc. 51 (2020) 1750, https://doi.org/10.1002/jrs.5677.

[30] R.N. Clark, G.A. Swayze, R.A. Wise, K.E. Livo, T.M. Hoefen, R.F. Kokaly, S. J. Sutley, USGS digital spectral library splib06a, Dig.Ser. 231 (2007), https://doi.org/10.3133/ds231.

[31] E.A. Cloutis, M.A. Craig, R.V. Kruzelecky, W.R. Jamroz, A. Scott, F.C. Hawthorne, S.A. Mertzman, Spectral reflectance properties of minerals exposed to simulated Mars surface conditions, Icarus 195 (2008) 140, https://doi.org/10.1016/j.icarus.2007.10.028.

[32] B. Lafuente, R.T. Downs, H. Yang, N. Stone, Highlights in Mineralogical Crystallography, Armbruster, De Gruyter, Berlin, 2015.

[33] J.A. Manrique, J. Santamaria-Sancho, G. Lopez-Reyes, M. Veneranda, G. Arana, K. Castro, J.M. Madariaga, S. Maurice, C. Prieto-Garcia, F. Rull, A. Sanz-Arranz, R. C. Wiens, S. Team, Evaluation of similitudes between SuperCam and SimulCAm, a laboratory standoff setup for support science, in: 53rd Lunar Planet. Sci. Conf., The Woodlands, Houston, USA, 2022, p. 2589. Abs.

[34] F. Rull, S. Maurice, I. Hutchinson, A. Moral, C. Perez, C. Diaz, M. Colombo, T. Belenguer, G. Lopez-Reyes, A. Sansano, O. Forni, Y. Parot, N. Striebig, S. Woodward, C. Howe, N. Tarcea, P. Rodriguez, L. Seoane, A. Santiago, J. A. Rodriguez-Prieto, J. Medina, P. Gallego, R. Canchal, P. Santamaría, G. Ramos, J. L. Vago, On behalf of the RLS team, the Raman laser spectrometer for the ExoMars rover mission to Mars, Astrobiology 17 (2017) 627, https://doi.org/10.1089/ast.2016.1567.

[35] G. Lopez-Reyes, F. Rull Pérez, A method for the automated Raman spectra acquisition, J. Raman Spectrosc. 48 (2017) 1654, https://doi.org/10.1002/jrs.5185.

[36] M. Veneranda, A. Sanz-Arranz, J.A. Manrique, J. Saiz, C. Garcia-Prieto, E. Pascual-Sánchez, J. Medina, M. Konstantinidis, E. Lalla, A. Moral, L.M. Nieto, F. Rull, G. Lopez-Reyes, Analytical database of Martian minerals (ADaMM): project synopsis and Raman data overview, J. Raman Spectrosc. 53 (2022) 364, https://doi.org/10.1002/jrs.6215.

[37] L. Sánchez-García, C. Aeppli, V. Parro, D. Fernández-Remolar, M. García-Villadangos, G. Chong-Diaz, Y. Blanco, D. Carrizo, Molecular biomarkers in the subsurface of the Salar Grande (Atacama, Chile) evaporitic deposits, Biogeochemistry 140 (2018) 31, https://doi.org/10.1007/s10533-018-0477-3.

[38] R. Grimalt, C. Gelmetti, Eruptive vellus hair cysts: case report and review of the literature, Pediatr. Dermatol. 9 (1992) 98, https://doi.org/10.1111/j.1525-1470.1992.tb01222.x.

[39] D. Carrizo, L. Sánchez-García, R.J. Menes, F. García-Rodríguez, Discriminating sources and preservation of organic matter in surface sediments from five Antarctic lakes in the Fildes Peninsula (King George Island) by lipid biomarkers and compound-specific isotopic analysis, Sci. Total Environ. 672 (2019) 657, https://doi.org/10.1016/j.scitotenv.2019.03.459.

[40] L. Sánchez-García, D. Carrizo, A. Molina, V. Muñoz-Iglesias, M.Á. Lezcano, M. Fernández-Sampedro, V. Parro, O. Prieto-Ballesteros, Fingerprinting molecular and isotopic biosignatures on different hydrothermal scenarios of Iceland, an acidic and sulfur-rich Mars analog, Sci. Rep. 10 (2020), 21196, https://doi.org/10.1038/s41598-020-78240-2.

[41] V. Megevand, D. Carrizo, M.Á. Lezcano, M. Moreno-Paz, N.A. Cabrol, V. Parro, L. Sánchez-García, Lipid profiles from fresh biofilms along a temperature gradient on a hydrothermal Stream at el tatio (Chilean Andes), as a proxy for the interpretation of past and present biomarkers beyond Earth, Front. Microbiol. 13 (2022), 811904, https://doi.org/10.3389/fmicb.2022.811904.

[42] T.A. Abrajano, D.E. Murphy, J. Fang, P. Comet, J.M. Brooks, Ratios in individual fatty acids of marine mytilids with and without bacterial symbionts, Org. Geochem. 21 (1994) 611, https://doi.org/10.1016/0146-6380(94)90007-8.

[43] V. Lazic, A. Palucci, S. Jovicevic, C. Poggi, E. Buono, Analysis of explosive and other organic residues by laser induced breakdown spectroscopy, Spectrochim. Acta Part B At. Spectrosc. 64 (2009) 1028, https://doi.org/10.1016/j.sab.2009.07.035.

[44] J. Moros, J. Laserna, Laser-induced breakdown spectroscopy (LIBS) of organic compounds: a review, Appl. Spectrosc. 73 (2019) 963, https://doi.org/10.1177/0003702819853252.

[45] K. Janiszewska, M. Mazur, M. Machalski, J. Stolarski, From pristine aragonite to blocky calcite: exceptional preservation and diagenesis of cephalopod nacre in porous Cretaceous limestones, PLoS One 13 (2018), e0208598, https://doi.org/10.1371/journal.pone.0208598.

[46] L. Borromeo, U. Zimmermann, S. Andò, G. Coletti, D. Bersani, D. Basso, P. Gentile, B. Schulz, E. Garzanti, Raman spectroscopy as a tool for magnesium estimation in Mg-calcite, J. Raman Spectrosc. 48 (2017) 983, https://doi.org/10.1002/jrs.5156.

[47] J. Perrin, D. Vielzeuf, D. Laporte, A. Ricolleau, G.R. Rossman, N. Floquet, Raman characterization of synthetic magnesian calcites, Am. Mineral. 101 (2016) 2525, https://doi.org/10.2138/am-2016-5714.

[48] J. Greinert, G. Bohrmann, M. Elvert, Stromatolitic fabric of authigenic carbonate crusts: result of anaerobic methane oxidation at cold seeps in 4,850 m water depth, Int. J. Earth Sci. 91 (2002) 698, https://doi.org/10.1007/s00531-001-0244-9.

[49] C.L. Pederson, D.F. McNeill, J.S. Klaus, P.K. Swart, Deposition and diagenesis of marine oncoids: implications for development of carbonate porosity, J. Sediment. Res. 85 (2015) 1323, https://doi.org/10.2110/jsr.2015.77.

[50] A. Wang, B.L. Jolliff, L.A. Haskin, K.E. Kuebler, K.M. Viskupic, Characterization and comparison of structural and compositional features of planetary quadrilateral pyroxenes by Raman spectroscopy, Am. Mineral. 86 (2001) 790, https://doi.org/10.2138/am-2001-0703.

[51] J.J. Freeman, A. Wang, K.E. Kuebler, B.L. Jolliff, LaA. Haskin, Characterization of natural feldspars by Raman spectroscopy for future planetary exploration, Can. Mineral. 46 (2008) 1477, https://doi.org/10.3749/canmin.46.6.1477.
[52] L. Heindel, D. Birgel, J. Peckmann, H. Kuhnert, H. Westphal, Formation of deglacial microbialites in coral reefs off Tahiti (IODP 310) involving sulfate-reducing bacteria, Palaios 25 (2010) 618, https://doi.org/10.2110/palo.2010.p10-032r.
[53] Y.D. Winters, T.K. Lowenstein, M.N. Timofeeff, Identification of carotenoids in ancient salt from death valley, saline valley, and searles lake, California, using laser Raman spectroscopy, Astrobiology 13 (2013) 1065, https://doi.org/10.1089/ast.2012.0952.
[54] M.F.C. Verkaaik, J.-H. Hooijschuur, G.R. Davies, F. Ariese, Raman spectroscopic techniques for planetary exploration: detecting microorganisms through minerals, Astrobiology 15 (2015) 697, https://doi.org/10.1089/ast.2015.1329.
[55] J. Grimalt, I. Yruela, C. Saiz-Jimenez, J. Toja, J. de Leeuw, J. Albaigés, Sedimentary lipid biogeochemistry of an hypereutrophic alkaline lagoon, Geochem. Cosmochim. Acta 55 (1991) 2555, https://doi.org/10.1016/0016-7037(91)90373-D.
[56] R.C. Coates, S. Podell, A. Korobeynikov, A. Lapidus, P. Pevzner, D.H. Sherman, E. E. Allen, L. Gerwick, W.H. Gerwick, Characterization of cyanobacterial hydrocarbon composition and distribution of biosynthetic pathways, PLoS One 9 (2014), e85140, https://doi.org/10.1371/journal.pone.0085140.
[57] J.O. Grimalt, R. de Wit, P. Teixidor, J. Albaigés, Lipid biogeochemistry of phormidium and microcoleus mats, Org. Geochem. 19 (1992) 509, https://doi.org/10.1016/0146-6380(92)90015-.
[58] S.D. Killops, V.J. Killops, in: P. Farrimond (Ed.), An Introduction to Organic Geochemistry, Geol. Mag., 1994, p. 702, https://doi.org/10.1017/S0016756800012656.
[59] J. Kuever, The family syntrophaceae, in: The Prokaryotes, Springer Berlin Heidelberg, Berlin, Heidelberg, 2014, pp. 281–288, https://doi.org/10.1007/978-3-642-39044-9_269.
[60] N. Dijkman, J. Kromkamp, Phospholipid-derived fatty acids as chemotaxonomic markers for phytoplankton: application for inferring phytoplankton composition, Mar. Ecol. Prog. Ser. 324 (2006) 113, https://doi.org/10.3354/meps324113.
[61] J.M. Hayes, Fractionation of carbon and hydrogen isotopes in biosynthetic processes, Rev. Mineral. Geochem. 43 (2001) 225, https://doi.org/10.2138/gsrmg.43.1.225.
[62] M. Hügler, S.M. Sievert, Beyond the Calvin cycle: autotrophic carbon fixation in the ocean, Ann. Rev. Mar. Sci 3 (2011) 261, https://doi.org/10.1146/annurev-marine-120709-142712.
[63] R. Sirevg, B.B. Buchanan, J.A. Berry, J.H. Troughton, Mechanisms of CO2 fixation in bacterial photosynthesis studied by the carbon isotope fractionation technique, Arch. Microbiol. 112 (1977) 35, https://doi.org/10.1007/BF00446651.
[64] J.J. Brocks, G.D. Love, R.E. Summons, A.H. Knoll, G.A. Logan, S.A. Bowden, Biomarker evidence for green and purple sulphur bacteria in a stratified Palaeoproterozoic sea, Nature 437 (2005) 866, https://doi.org/10.1038/nature04068.
[65] C. Freissinet, D.P. Glavin, A. Buch, C. Szopa, S. Teinturier, D.P. Archer, A. J. Williams, R. Williams, M. Millan, A. Steele, R. Navarro-Gonzalez, C.H. House, C. A. Malespin, P. Mahaffy, Detection of long-chain hydrocarbons on Mars with the sample analysis at Mars (SAM) instrument, in: 9th Int. Conf. Mars, Abs, Pasadena, CA, USA, 2019, p. 6123.